Comparative high-pressure investigations of Ag_2ZnSnS_4 and Ag_2CdSnS_4 compounds

Nicole Yvonne Suss ; Eva M. Heppke ; Elena Voloshina ; Lukas Schifferle ; Sergey S. Lobanov ;
Sergio Speziale ; Hans Josef Reichmann ; Tim Küllmey ; Beate Paulus ; Martin Lerch ;
Ilias Efthimiopoulos

Check for updates

View Online   Export Citation   CrossMark

31 October 2023 05:52:40

Comparative high-pressure investigations of Ag$_2$ZnSnS$_4$ and Ag$_2$CdSnS$_4$ compounds

Nicole Yvonne Suss,[1,2] [iD] Eva M. Heppke,[2] [iD] Elena Voloshina,[3] [iD] Lukas Schifferle,[1,4] [iD]
Sergey S. Lobanov,[1,4] [iD] Sergio Speziale,[1] [iD] Hans Josef Reichmann,[1] [iD] Tim Küllmey,[3] [iD]
Beate Paulus,[3,a] [iD] Martin Lerch,[2] [iD] and Ilias Efthimiopoulos[1,a),b)] [iD]

AFFILIATIONS

[1] GFZ German Research Center for Geosciences, Telegrafenberg, 14473 Potsdam, Germany
[2] Institut für Chemie, Technische Universität Berlin, Straße des 17.Juni 135, 10623 Berlin, Germany
[3] Institut für Chemie und Biochemie, Freie Universität Berlin, Arnimallee 22, 14195 Berlin, Germany
[4] Institut für Geowissenschaften, Universität Potsdam, Karl-Liebknecht-Str. 24-25, Golm, Potsdam 14476, Germany

[a)] Author to whom correspondence should be addressed: b.paulus@fu-berlin.de and iliefthi@gfz-potsdam.de.
[b)] Present address: Max-Planck-Institut für Eisenforschung GmbH, Max-Planck-Str. 1, 40237 Düsseldorf, Germany.

ABSTRACT

Quaternary kesterite-type (KS) compounds have attracted worldwide attention from the scientific community as promising materials for solar cells. On the route to optimizing their performance, the effect of stress and strain constitutes a critical factor when it comes to thin film applications. Following a recent theoretical study, we report here joint experimental and computational high-pressure investigations on the KS Ag$_2$ZnSnS$_4$ and wurtz–kesterite (WZ–KS)-type Ag$_2$CdSnS$_4$ compounds. Our results reveal that both materials undergo successive transformations, first into a GeSb-type and then toward a CrN-type modification at ambient temperature. Our theoretical calculations predict a metallic character for all Ag$_2$ZnSnS$_4$ and Ag$_2$CdSnS$_4$ high-pressure phases. In addition, structural disorder is observed in KS Ag$_2$ZnSnS$_4$ upon moderate compression, prior to its KS → GeSb-type transition. Decompression leads to the recovery of a disordered zinc blende-type structure in the latter, whereas Ag$_2$CdSnS$_4$ retains the disordered GeSb-type modification. The similarities and deviations from the archetypical KS Cu$_2$ZnSnS$_4$ are discussed.

I. INTRODUCTION

The series of quaternary semiconducting $A_2^I B^{II} C^{IV} X_4$ chalcogenides (X = S, Se, Te) has attracted significant attention recently, driven mainly by their potential use as photoabsorbing thin films in solar cells.[1–6] The "lion's share" of the conducted investigations belongs to the Cu^{1+}-bearing materials, as they exhibit the most promising photovoltaic properties due to their high absorption coefficients in the visible range ($\sim 10^4$ cm^{-1}) and almost optimal band gaps ($E_g \approx 1.5$ eV).[6,7] A detrimental factor for applications, however, is the presence of various intrinsic defects (e.g., cationic disorder and vacancies) and/or secondary phases arising from the preparation methods of these compounds.[8–14]

One of the commonly used practices to circumvent these shortcomings is isovalent cationic substitution, with the versatility of the structure allowing for a multitude of options.[1,15–25] For example, it has been shown that exchanging Cu^{1+} with the larger Ag^{1+} (A site) or Zn^{2+} with the larger Cd^{2+} cations (B site) leads to a considerable suppression of the formation of intrinsic defects, thus pointing toward an effective way to enhance the photovoltaic efficiency of these compounds.[11,20,26–30]

Another key factor influencing the application-oriented properties of these materials is the response to stress and strain conditions induced, for instance, by the lattice mismatch between the thin film and the underlying substrate.[31–34] The only known experimental high-pressure studies conducted on these systems are on kesterite-type (KS) Cu$_2$ZnSnS$_4$.[35–38] In these investigations, it has been established that pressure leads first to a disordering of the KS structure (DKS), followed by a transformation toward a disordered GeSb-type phase. These structural transitions are accompanied by concomitant

changes in the respective electronic properties, i.e., an insulator-to-metal transition, which is expected to affect in turn the photovoltaic performance.[39–41] A similar pressure-induced transition sequence was recently predicted for two more relevant materials, namely Ag_2ZnSnS_4 and Ag_2CdSnS_4.[42]

Regarding the former compound, except for the aforementioned benefits of the Cu^{1+}/Ag^{1+} substitution suppressing intrinsic defects, the Ag_2ZnSnS_4 end-member has also shown promising photocatalytic properties.[43–46] The structure of Ag_2ZnSnS_4 at ambient conditions has been debated in the literature, as both a KS (Fig. 1) and a stannite-type (ST) modification have been proposed.[23,30,42,47] The two structures differ in the cationic layer ordering motif (KS: alternating Ag/Sn and Ag/Zn; ST: Ag and Zn/Sn)[48] and lie energetically close to each other from a computational perspective. Nevertheless, the majority of investigations tend to favor the KS phase as the stable Ag_2ZnSnS_4 modification at ambient conditions.[23,42,43]

On the other hand, Ag_2CdSnS_4 appears to be a promising candidate for optoelectronic applications, with a bandgap close to ~1.9 eV.[49] This material adopts the wurtz–kesterite (WZ–KS) type structure at ambient conditions (Fig. 1).[50] The structure of this phase bears some resemblance to that of KS in that it is composed of alternating Ag/Cd and Ag/Sn layers; however, the hexagonal close packed arrangement of the sulfur anions results in a wurtzite-like honeycomb set-up. It is worth mentioning here that KS originates from the cubic diamond structure, whereas WZ–KS comes from the hexagonal diamond polymorph.[50] Heating above 470 K transforms Ag_2CdSnS_4 into a (quenchable) wurtz–stannite-type structure.[50]

Given that the *P-T* phase diagram for this class of materials remains largely unexplored, an experimental verification of the predicted structural transformations[42] of Ag_2ZnSnS_4 and Ag_2CdSnS_4 is important for understanding the structural systematics in this material family under compression. Our results point

to a more complex phase diagram under pressure than originally envisioned for these materials, including the investigated Cu_2ZnSnS_4.[35–38,42]

II. EXPERIMENTAL AND COMPUTATIONAL DETAILS

The Ag_2ZnSnS_4 and Ag_2CdSnS_4 samples were available in powdered polycrystalline form. Synthesis details for Ag_2CdSnS_4 can be found in Ref. 50. For the preparation of Ag_2ZnSnS_4, the starting materials Ag_2S, SnS, ZnS, and S were mixed in a stoichiometric ratio and milled in a planetary mono mill operating at 400 rpm for 3 h. An annealing step at 600 °C in an H_2S atmosphere for 2 h inside a silica glass tube furnace after milling served to improve the crystallinity of the material. The final Ag_2ZnSnS_4 product was characterized with X-ray diffraction (XRD), Energy-dispersive X-ray (EDX) spectroscopy, Ultraviolet–Visible (UV–VIS) absorbance, and Raman spectroscopic methods (Figs. S1 and S2 and Tables S1–S6 in supplementary material). Even though our characterization methods do not allow for a definite assignment of the synthetic Ag_2ZnSnS_4 to either the KS or the ST phase, we favor the KS structure based mainly on literature consensus.[23,42,43]

Pressure was generated with symmetric diamond anvil cells (DACs) equipped with diamonds of 300–400 μm culet diameters. Drilled pre-indented rhenium gaskets with hole diameters of 150–200 μm served as sample chambers in separate runs. Cryogenically loaded argon served as a pressure transmitting medium (PTM) in all experiments. The ruby luminescence method was used for measuring pressure.[51]

The high-pressure Raman measurements were conducted with a Horiba Jobin Yvon LabRam HR800 UV–VIS single-stage Raman spectrometer equipped with a HeNe laser (λ = 633 nm), a 10× long-working distance objective lens, an 1800 l/mm diffraction grating, and a Peltier-cooled charge-coupled device (CCD) detector
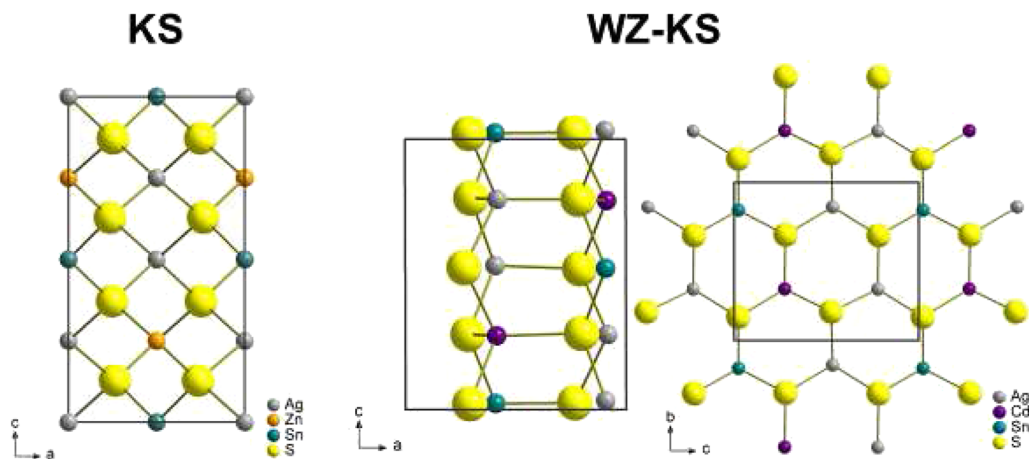
FIG. 1. Crystal structures for the starting phases of Ag_2ZnSnS_4 (KS, SG $I\bar{4}$, Z = 2, left) and Ag_2CdSnS_4 (WZ–KS, SG *Pn*, Z = 2, right). The KS and WZ–KS structures are projected along the $[0\bar{1}0]$ and $[\bar{1}00]$ directions for better viewing of the alternating cation/anion layers. The Ag, Zn, Cd, Sn, and S atoms are represented by gray, orange, purple, green, and yellow spheres, respectively.

(1024 × 256 pixels). The measured frequency range was 100–500 cm^{-1}, with the spectra being collected with varying times, ranging from 60 s (lower pressure) to 240 s (higher pressure), averaged over three accumulations each. The incident laser power was kept below 1 mW in order to avoid any laser-induced damage to the sample.[52] The Raman-relevant parameters were obtained from the fitting of the Raman spectra with Lorentzian functions, accompanied by linear background correction/subtraction using the Fityk 1.3.1 software.[53]

Angle-resolved high-pressure powder XRD measurements were performed at the Extreme Conditions Beamline P02.2 of PETRA III (Hamburg, Germany)[54] with an incident X-ray wavelength $\lambda = 0.2903$ Å and a beam size of 2×2 μm^2. Two-dimensional XRD patterns were collected with a fast flat panel detector XRD1621 from PerkinElmer (2048 pixels × 2048 pixels, 200×200 μm^2 pixel size) and processed with the FIT2D software.[55] Refinements were performed using the GSAS + EXPGUI software packages.[56] The Birch–Murnaghan equation of state (B–M EOS) function[57,58] was fitted to the obtained pressure-volume (P–V) data of each phase. Given that the Ar PTM becomes solid at 1.4 GPa after crystallizing in a fcc-structured phase,[59] we used the fcc-Ar EOS as an additional pressure calibrant.[60,61]

Density functional theory (DFT) calculations based on plane-wave basis sets of 700 eV cutoff energy were performed with the Vienna *ab initio* simulation package (VASP).[62,63] The Perdew–Burke–Ernzerhof (PBE) exchange-correlation functional[64] was employed. The electron–ion interaction was described within the projector augmented wave (PAW) method[65] with Ag ($4d$, $5s$), Zn ($3d$, $4s$), Cd ($4d$, $5s$), S ($2s$, $2p$), and Sn ($4d$, $5s$, $5p$) states treated as valence states. The Brillouin-zone integration was performed on Γ-centered symmetry reduced Monkhorst–Pack meshes using a Gaussian smearing with $\sigma = 0.01$ eV, except for the calculation of total energies and densities of states (DOSs). For those calculations, the tetrahedron method with Blöchl corrections[66] was employed. An $8 \times 8 \times 4$ k-mesh was used. The convergence criteria for energy were set equal to 10^{-5} eV. The pressure dependence was determined by selecting volume points in a range of about 40 Å^3 above and below the minima and a step size of 4 Å^3. At each constant volume, we optimized the ionic positions and cell shape until forces became smaller than 0.01 eV Å^{-1}. We fitted the total energy vs volume to a Birch–Murnaghan equation of state,[58]

$$E(V) = E_0 + \frac{9V_0B_0}{16}\left\{\left[\left(\frac{V_0}{V}\right)^{\frac{2}{3}} - 1\right]^3 B_0' + \left[\left(\frac{V_0}{V}\right)^{\frac{2}{3}} - 1\right]^2 \times \left[6 - 4\left(\frac{V_0}{V}\right)^{\frac{2}{3}}\right]\right\}, \quad (1)$$

where E_0 denotes the energy per unit cell at zero pressure, V_0 is the reference volume at zero pressure, B_0 is the bulk modulus at zero pressure, and B_0' is its pressure derivative. Then, the pressure at each volume was obtained according to the formula

$$P(V) = \frac{3B_0}{2}\left[\left(\frac{V_0}{V}\right)^{\frac{7}{3}} - \left(\frac{V_0}{V}\right)^{\frac{5}{3}}\right] \times \left\{1 + \frac{3}{4}\left(B_0' - 4\right)\left[\left(\frac{V_0}{V}\right)^{\frac{2}{3}} - 1\right]\right\}. \quad (2)$$

III. RESULTS AND DISCUSSION
A. High-pressure behavior of Ag$_2$ZnSnS$_4$

Our high-pressure Raman investigations on Ag$_2$ZnSnS$_4$ are summarized in Fig. 2. In the KS phase, a total of 15 Raman-active modes are predicted,[67]

$$\Gamma = 3\,A + 6\,B + 6\,E. \quad (3)$$

At ambient conditions, the measured Ag$_2$ZnSnS$_4$ Raman spectrum is composed mainly of two intense Raman modes (272 and 347 cm^{-1}) and three weaker features, in agreement with earlier reports.[47,68,69] Even though the vibrational properties of KS Ag$_2$ZnSnS$_4$ have not been investigated, we can assign all of the observed Raman bands following the relevant results on KS Cu$_2$ZnSnS$_4$ (Table S6 in supplementary material).[70–72] For example, the two most intense Raman bands at 272 and 347 cm^{-1} should correspond to A-symmetry sulfur vibrations along the *ab*-plane and the *c*-axis, respectively. In addition, we detected a "shoulder" band at 343 cm^{-1}, not reported before for Ag$_2$ZnSnS$_4$; the origin of this feature is unclear, yet its behavior under pressure hints at a close connection to a similar Raman sideband observed in KS Cu$_2$ZnSnS$_4$.[36,37] We return to this point later.

Upon pressure increase, all of the Raman-active vibrations shift to higher frequencies with similar pressure rates [Fig. 2(b) and Table S6 in the supplementary material]. Interestingly, the pressure slopes determined for KS Ag$_2$ZnSnS$_4$ are very close to the respective pressure rates of the Raman-active modes of KS Cu$_2$ZnSnS$_4$,[37] indicating a similar compression mechanism for both compounds.

The most notable observation in our Raman studies, however, is the behavior of the unassigned 343 cm^{-1} sideband. Upon pressure increase, this sideband enhances progressively intensity-wise at the expense of its adjacent 347 cm^{-1} peak, surpassing it after ~3 GPa [Figs. 2(c) and S3 in supplementary material]. The effect strongly resembles the pressure-induced behavior reported for KS Cu$_2$ZnSnS$_4$, where the progressive intensity enhancement of a similar sideband at the expense of its adjacent (and initially intense) A mode was found.[37] In KS Cu$_2$ZnSnS$_4$, this sideband has been associated with the presence of cationic exchange/local structural disorder.[52,73,74] From this similarity alone, we can reasonably infer that the 343 cm^{-1} sideband in Ag$_2$ZnSnS$_4$ arises due to similar reasons, with pressure promoting it further, as in Cu$_2$ZnSnS$_4$.[37]

An overall Raman intensity drop is detected at 5.8–6.9 GPa, followed by an *irreversible* loss of Raman signal at 8.3 GPa. The loss of the Raman signal points to a pressure-induced phase transition in Ag$_2$ZnSnS$_4$. Possible reasons explaining the drastic reduction/vanishing of the Raman intensity include structural disorder, adoption of a high-symmetry (i.e., Raman-inactive) phase, and/or enhancement of conductivity (metallization).

The first two scenarios concern the structural properties of the material and can be resolved by high-pressure XRD investigations. In Fig. 3(a), we show the XRD patterns of Ag$_2$ZnSnS$_4$ collected at various pressures. We find that the KS phase reproduces the experimental XRD patterns up to 7.1 GPa, although not perfectly [Fig. 3(b)]. The reason is the splitting of the most intense XRD feature close to $2\theta \approx 5°$, assigned to the KS 112 Bragg peak (Fig. S4 in supplementary material); due to the relatively low intensity and broadness of the remaining XRD features, no further "structural inconsistencies" with the KS phase could be identified.
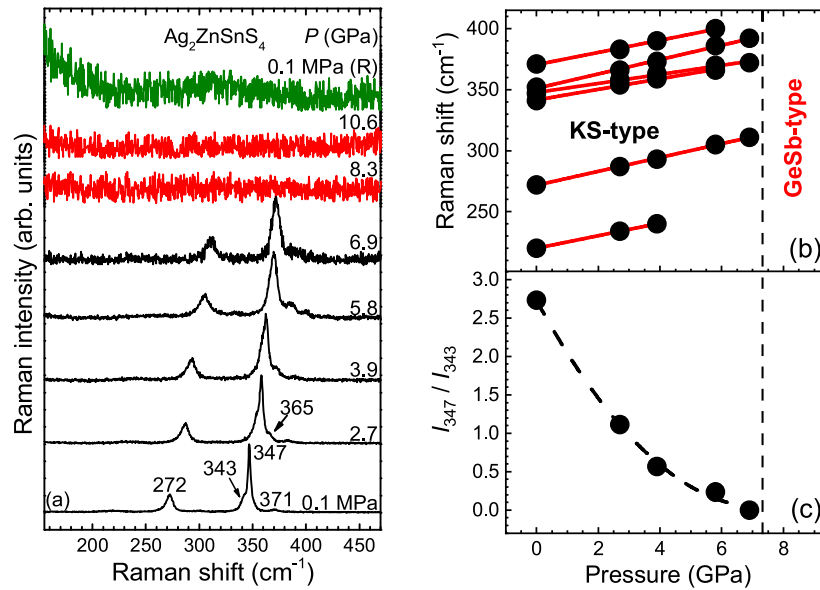
FIG. 2. (a) Raman spectra of Ag_2ZnSnS_4 at various pressures (λ = 633 nm, T = 300 K). The black, red, and green colors stand for the starting KS-type, the high-pressure GeSb-type, and the recovered zinc-blende (ZB-type) phases, respectively. (b) Raman mode frequencies of Ag_2ZnSnS_4 as a function of pressure. The red solid lines passing through the data indicate the least square fittings (Table S6 in the supplementary material). (c) Pressure dependence of the integrated Raman intensity ratio of the Ag_2ZnSnS_4 Raman bands with frequencies of 347 and 343 cm^{-1} (ambient pressure values). The vertical dashed line denotes the KS $\rightarrow$ GeSb-type structural transition. Fitting examples are shown in Fig. S3 in the supplementary material.
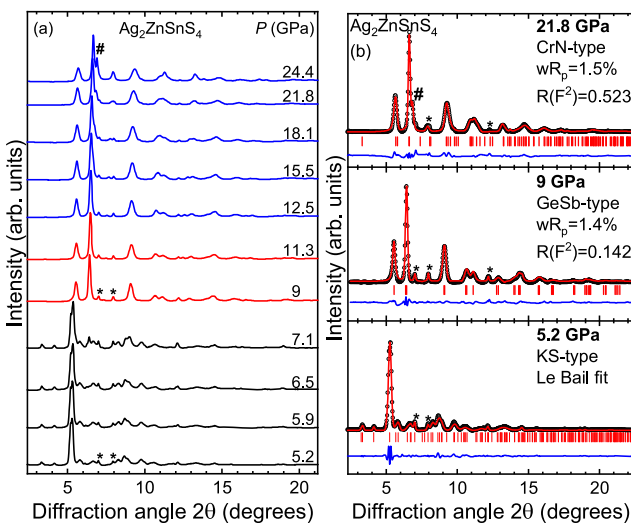

FIG. 3. (a) Selected XRD patterns of Ag_2ZnSnS_4 at various pressures (T = 300 K, λ = 0.2903 Å). The various phases are indicated by black (KS), red (GeSb-type), and blue (CrN-type) colors. (b) Refined XRD patterns for the KS (5.2 GPa, Le Bail, bottom), the GeSb-type (9 GPa, Rietveld, middle), and the CrN-type (21.8 GPa, Rietveld, top) phases of Ag_2ZnSnS_4. Dots correspond to the experimental data, and the red solid lines represent the best refinements. The difference spectra between the measured and simulated patterns are depicted as blue curves. Vertical ticks mark the respective Bragg peak positions of the Ag_2ZnSnS_4 polymorphs. The strongest Bragg features of the rhenium gasket material (asterisks) and the argon PTM (#) are also noted.

One might attribute this splitting to the presence of an impurity, but due to the absence of a secondary phase from the starting XRD pattern (Fig. S1 in the supplementary material), we find this scenario unlikely. On the contrary, considering our Raman study [Fig. 2(c)], we tend to assign this Bragg peak splitting as a sign of structural disorder. Actually, a close inspection of the EDX results (Table S5 in the supplementary material) hints to the potential presence of an L-type (or J-type) disorder in Ag_2ZnSnS_4 at ambient conditions, i.e., the partial exchange of Ag^+ cations from a mixture of Zn^{2+} and Sn^{4+} (or Sn^{4+} and Ag^+ vacancies).[75]

Taken together, a plausible scenario might be that such a disorder has escaped detection in the Ag_2ZnSnS_4 XRD pattern at ambient conditions (Fig. S1 in the supplementary material), but is identified by Raman spectroscopy, a more local structural probe, and its fingerprint being the 343 cm^{-1} sideband [Fig. 2(a)]. An increase in pressure results in the progressive promotion of the structural disorder at the expense of the KS phase, as revealed by the respective Raman intensity ratio [Fig. 2(c)]. According to the latter, the disordered phase should become more favorable above 3 GPa, consequently large enough volume-wise to be detected in the 5.2 GPa XRD pattern via the Bragg peak splitting [Fig. 3(a)].

Another interesting aspect is that the two Bragg peak constituents show different pressure rates, with the high-angle component exhibiting an almost doubled pressure slope compared to its adjacent low-angle Bragg feature (termed d_2 and d_1, respectively; Fig. S4 in the supplementary material). Furthermore, the d_2 peak appears to enhance intensity-wise under pressure with respect to d_1 (Fig. S4 in the supplementary material). Considering also that none of the disordered structures described for Cu_2ZnSnS_4 alone can

reproduce the splitting of this particular Bragg peak in Ag_2ZnSnS_4,[75] a plausible scenario might be that the d_1 and d_2 Bragg peaks belong actually to *two separate phases*. This means that from 5.2 GPa and onwards, two distinct yet structurally similar phases coexist in Ag_2ZnSnS_4: the starting KS modification and a variant of the latter (e.g., a stannite-type phase component). Such a scenario has already been discussed for Cu_2ZnSnS_4 at ambient conditions.[13,14] Another possibility might be that Ag_2ZnSnS_4 has adopted a low-symmetry phase (e.g., orthorhombic), which nevertheless lies structurally close to the starting KS modification. For example, recent calculations on Ag_2ZnSnS_4 have shown that the WZ–KS phase lies energetically close to the KS modification for an extended pressure range,[42] hinting that a possible pressure-induced connection between the two structures might exist under certain prerequisites; the adoption of a WZ–KS-like variant in Ag_2ZnSnS_4 may be further advocated by the close resemblance of the Ag_2ZnSnS_4 and Ag_2CdSnS_4 Raman spectra [Figs. 2(a) and 5(a)]. Unfortunately, the measured data do not allow for a particular and definite identification of the disorder motif at this stage, and the aforementioned discussion remains rather speculative at this stage. Consequently, we fitted the XRD patterns up to 7.1 GPa, assuming a KS tetragonal cell [Fig. 3(b)]. This admission from our side led to satisfactory Le Bail refinements, yet with relatively large errors in structural parameters, as we discuss later below.

At 9 GPa, the Ag_2ZnSnS_4 XRD patterns change significantly, indicating a structural transition [Fig. 3(a)]. The transition pressure coincides roughly with the vanishing of the Raman signal [Fig. 2(a)]. The new phase could be indexed to a GeSb-type structure [Fig. 3(b)], a tetragonally distorted variant of the NaCl-type phase, in agreement with theoretical expectations.[42] In this phase, the involved Ag, Zn, and Sn cations occupy a single Wyckoff site, i.e., it is actually a disordered phase, whereas the coordination with respect to the sulfur anions has now increased from fourfold to sixfold.

Above 12.5 GPa, however, the GeSb-type structural model could no longer accurately reproduce the XRD patterns. Careful inspection of the XRD patterns indicated that a further distortion of the tetragonal unit cell should be used for properly reproducing the experimental XRD diffractograms, i.e., an orthorhombic phase (Fig. S5 in supplementary material). Examination of the possible GeSb-type orthorhombic subgroups resulted in using a CrN-type phase as a structural model. The latter represents an orthorhombically distorted variant of the NaCl-type phase[76] and provides reliable refinements up to the highest experimental pressure [Fig. 3(b)].

It should be pointed out that both Ag_2ZnSnS_4 high-pressure modifications are expected to show Raman activity;[77] hence, the vanishing of the Raman signal is most likely originating from a change in the electronic properties of Ag_2ZnSnS_4 arising from the aforementioned structural alterations. This aspect is supported by calculations, as we show later.

Experimental unit-cell parameters are plotted as a function of pressure in Figs. 4(a) and 4(b). We can readily observe that the KS → GeSb-type transformation displays a ~11% volume drop at the transition point, associated with the cationic coordination increase from fourfold to sixfold.[35–37] On the other hand, the GeSb- → CrN-type transition does not show any visible volume difference at the transition point, i.e., the two phases can be described by the same EoS function [Fig. 4(b) and Table I].
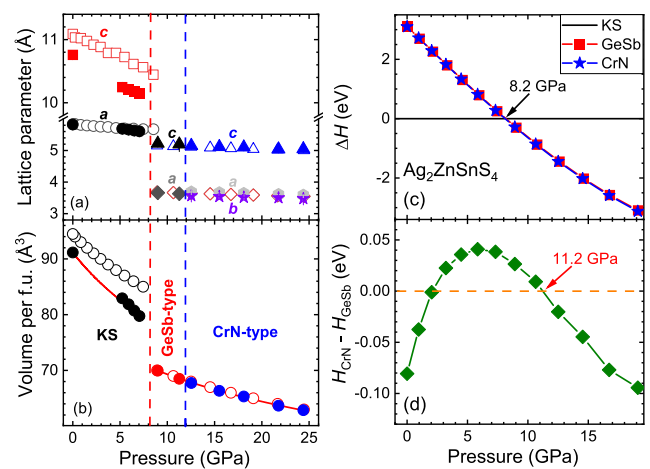

FIG. 4. (a) Lattice constants and (b) unit cell volume per formula unit (f.u.) as a function of pressure for the various polymorphs of Ag_2ZnSnS_4. Closed and open symbols correspond to experimental and DFT-calculated data (Tables S7 and S8 in the supplementary material). Error bars lie within the symbols. The vertical dashed lines mark the onset pressures of the successive KS → GeSb-type and GeSb- → CrN-type structural transitions. Solid red lines represent fitted Birch–Murnaghan EoS functions. (c) Calculated enthalpy difference ΔH between the high-pressure phases (GeSb-type in red, CrN-type in blue) and the starting KS (black line) modification of Ag_2ZnSnS_4. (d) Enthalpy difference between the GeSb-type and CrN-type modifications of Ag_2ZnSnS_4. A phase is stable if it has a lower value of H (KS and GeSb-type data from Ref. 42). The respective total energy values per unit cell are listed in Table S8 in the supplementary material.

Turning now to our calculations, Fig. 4(c) shows the enthalpy difference plots as a function of pressure for all of the aforementioned Ag_2ZnSnS_4 polymorphs, i.e., the KS, GeSb-type, and CrN-type structures. The GeSb-type and CrN-type modifications become energetically favorable at 8.2 GPa compared to the starting KS phase, as indicated by the lower enthalpies. Even though, at first glance, the GeSb-type and CrN-type enthalpies appear almost identical, plotting the relative enthalpy difference between these two high-pressure Ag_2ZnSnS_4 structures clearly shows that the CrN-type phase becomes the stable modification above 11.2 GPa compared to the GeSb-type. In summary, our calculations reveal the following sequence of pressure-induced structural transitions for Ag_2ZnSnS_4, fully supporting our experimental observations: the KS → GeSb-type transition takes place at 8.2 GPa, and the following GeSb- → CrN-type transition occurs at 11.2 GPa. The calculated transition pressure values are in very good agreement with the experimental observations (Fig. 4).

Finally, we compare the experimental and calculated structural parameters for the various Ag_2ZnSnS_4 phases [Figs. 4(a) and 4(b)]. In the KS structure, we can readily observe that despite the very good agreement of the *a*-axis, the experimental and computational *c*-axis (and volume) exhibit visible differences in their values. Except for the deviations arising from the approximations within DFT,[78] another plausible reason might be the choice of a single KS structural model for refining the Ag_2ZnSnS_4 XRD patterns (Figs. 3 and S4 in supplementary material). Indeed, this admission leads to a range of *c*-axis (and volume) values that can be acquired from Le

TABLE I. Volume per formula unit V/f.u., bulk modulus B_0, and its pressure derivative B'_0 for the various polymorphs of Ag_2ZnSnS_4 and Ag_2CdSnS_4 compounds at the respective reference pressures P_R, as obtained by fitting Birch–Murnaghan's function[57,58] to our measured (P–V) and computed (E-V) data. The term "fixed" means that the corresponding parameter was not allowed to vary during the EoS fitting.

Compound	Phase	P_R (GPa)	V/f.u. (Å^3)	B_0 (GPa)	B'_0	Method
Ag_2ZnSnS_4	KS	10^{-4}	182.3	41.9(9)	4 (fixed)	Exp.
	KS	10^{-4}	188.8	54.61	4.5	Calc.
	GeSb	9	139.9	105(6)	5.8(8)	Exp.
	GeSb	10^{-4}	154.03	76.21	4.65	Calc.
	CrN	10^{-4}	153.9	74.63	4.92	Calc.
Ag_2CdSnS_4	WZ–KS	10^{-4}	202.06	49.5	5.1	Calc.
	GeSb	4.8	151.3	71.4(8)	10.8(5)	Exp.
	GeSb	10^{-4}	161.89	71.72	4.83	Calc.
	CrN	12.3	140.6	259(8)	4 (fixed)	Exp.
	CrN	10^{-4}	161.68	71.41	4.97	Calc.
Cu_2ZnSnS_4[36,37]	KS	10^{-4}	160.1	74(2)	4.4(4)	Exp.
	KS	10^{-4}	163.75	68.64	4.64	Calc.
	GeSb	15.8	119.4	213(4)	4 (fixed)	Exp.
	GeSb	10^{-4}	120.75	82.16	4.57	Calc.

Bail refinements. Such a value range leads in turn to relatively large error bars in the respective experimental lattice parameters (Table S7 in the supplementary material), accounting for the noticeable discrepancy in the volume compressibility behavior [Fig. 4(b)]. On the contrary, the experimental and calculated parameters for the high-pressure GeSb-type and CrN-type modifications of Ag_2ZnSnS_4 show excellent agreement [Figs. 4(a) and 4(b)].

B. Pressure-induced evolution of Ag_2CdSnS_4

Having established the pressure-induced structural behavior of Ag_2ZnSnS_4, we move now to Ag_2CdSnS_4. In Fig. 5(a), we present our high-pressure Raman spectroscopic results. In the starting WZ–KS phase, a total of 48 Raman-active modes are predicted at the center of the Brillouin zone,[77]

$$\Gamma = 24A' + 24A''. \qquad (4)$$

The Raman spectrum of Ag_2CdSnS_4 at ambient conditions has not been reported before; hence, a unique assignment of the observed Raman features to specific mode symmetries is not possible at this stage. Interestingly, the Ag_2CdSnS_4 Raman response resembles closely that of Ag_2ZnSnS_4 [Figs. 2(a), S6 and Table S6 in supplementary material], comprising mainly two intense Raman features located at 251 and 344 cm^{-1}, with the latter displaying a sideband at 340 cm^{-1} [Fig. 5(a)]. Despite the different starting phases for the two compounds (Fig. 1), the similarity in Raman activity could be rationalized if we consider that WZ–KS and KS are structurally derived from the zinc-blende (ZB)-type and wurtzite (WZ)-type structures.[48,50] The latter, common polytypes for several binary materials (with ZnS constituting the most typical example), exhibit similar Raman activities.[79–81]

Upon pressure increase, the only observed change in the Ag_2CdSnS_4 Raman response is the shift of all the detected Raman features to higher frequencies (Fig. S6 in supplementary material). Unlike Ag_2ZnSnS_4, the relative intensity ratio of the prominent 344 cm^{-1} peak and its 340 cm^{-1} sideband does not vary upon compression [Fig. 5(a)]. On the other hand, the pressure slopes of the WZ–KS Ag_2CdSnS_4 Raman modes are very close to the respective KS Ag_2ZnSnS_4 ones (Table S6 in the supplementary material). This is again not surprising if we take into account the close proximity of the respective pressure slopes in the "parent" ZB and WZ polytypes.[82,83]

An overall Raman intensity drop initiates at 4.1 GPa, followed by a complete loss of Raman signal [Fig. 5(a)]. Upon full decompression, a weak and broad feature is observed in the Raman spectrum. Overall, Ag_2CdSnS_4 exhibits a similar high-pressure Raman response to Ag_2ZnSnS_4 (Fig. 2), implying a common high-pressure behavior of the two compounds.

The results of our XRD investigations are summarized in Fig. 5(b). The Ag_2CdSnS_4 XRD patterns collected at 4.8 GPa (the lowest pressure point in our dataset) can be indexed with a GeSb-type structure, confirming that the structural transformation of Ag_2CdSnS_4 from WZ–KS to GeSb-type is already completed at this pressure. Furthermore, compression leads to a subsequent structural transition of the GeSb-type modification toward a CrN-type phase at 12.3 GPa, persisting up to 25.4 GPa. Therefore, Ag_2CdSnS_4 exhibits a similar sequence of high-pressure structural transitions as Ag_2ZnSnS_4 (Fig. 3).

In Figs. 6(a) and 6(b), we plot the extracted Ag_2CdSnS_4 structural parameters for both the GeSb- and CrN-type high-pressure modifications. As revealed by the measured P–V data, there is no detectable volume drop at the GeSb- → CrN-type transition point. Unlike Ag_2ZnSnS_4, however, the GeSb- → CrN-type transition in

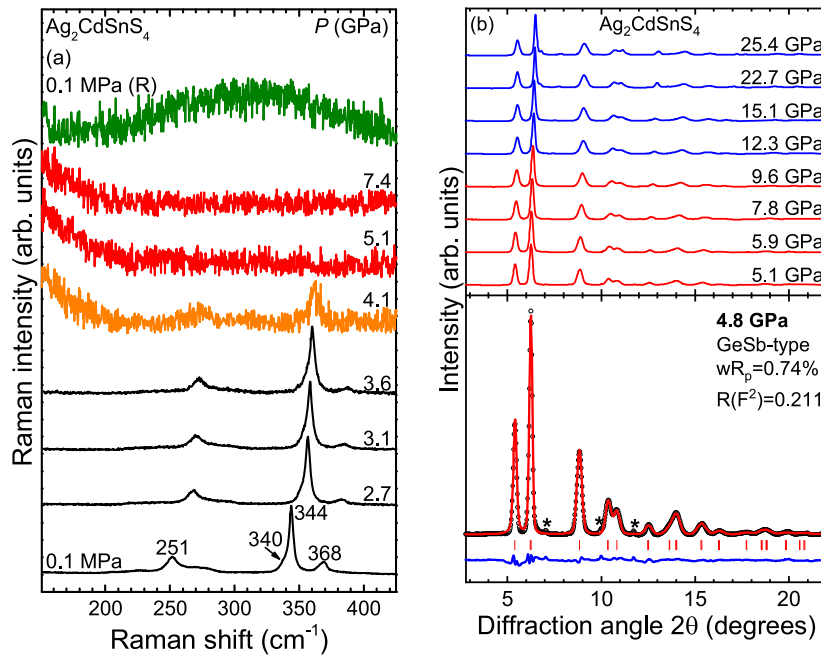**FIG. 5.** (a) Raman spectra of Ag_2CdSnS_4 at various pressures (λ = 633 nm, T = 300 K). The black, red, and green colors stand for the starting WZ–KS, the high-pressure GeSb-type, and the recovered GeSb-type phases, respectively; the orange color indicates the potential phase coexistence regime. The Raman mode frequencies of the strongest Raman-active features at ambient pressure are reported. (b) XRD patterns of Ag_2CdSnS_4 at various pressures (T = 300 K, λ = 0.2903 Å). The various phases are indicated by the red (GeSb-type) and blue (CrN-type) colors. Asterisks mark the strongest Bragg peaks of the Ar PTM. An example of a Rietveld refinement at 4.8 GPa is additionally presented (lower panel). Dots correspond to the measured pattern, and the red solid lines represent the best refinement. The difference curve between the measured and simulated patterns is depicted too (blue curves). Vertical ticks mark Bragg peak positions of the GeSb-type Ag_2CdSnS_4 phase.
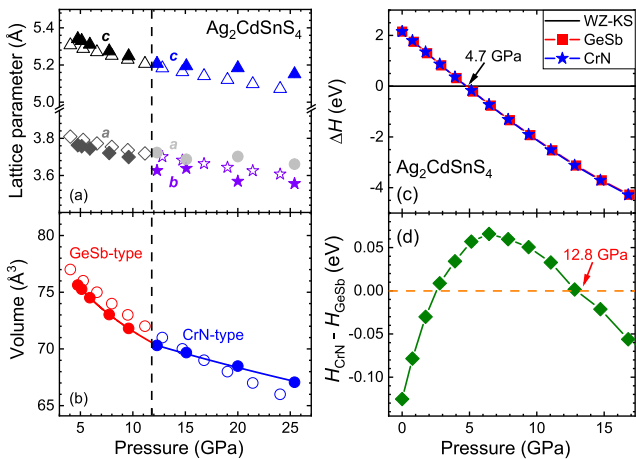

FIG. 6. (a) Lattice constants and (b) unit cell volume as a function of pressure for the high-pressure polymorphs of Ag_2CdSnS_4. Closed and open symbols correspond to experimental and DFT-calculated data (Tables S9 and S10 in the supplementary material). Error bars lie within the symbols. The vertical dashed line marks the onset pressure of the GeSb- → CrN-type structural transition. The solid lines represent fitted Birch–Murnaghan EoS functions. (c) Calculated enthalpy difference ΔH between the high-pressure polymorphs (GeSb-type: red; CrN-type: blue) and the starting WZ–KS (black line) of Ag_2CdSnS_4 as a function of pressure. (d) Enthalpy difference between the two high-pressure GeSb-type and CrN-type modifications. A phase is stable if it has a lower value of H (KS and GeSb-type data from Ref. 42). The respective total energy values per unit cell are listed in Table S10 in the supplementary material.

Ag_2CdSnS_4 is accompanied by a change in volume compressibility, i.e., the P–V data for the two phases can only be described by different sets of EoS coefficients [Fig. 6(b)]. Whether the volume compressibility change originates from inherent or extrinsic effects (e.g., the non-hydrostatic conditions imposed by the argon PTM at these pressures)[59] is not immediately obvious. Our calculations point to a relatively smooth GeSb- → CrN-type transition without a substantial compressibility change across the transition [open symbols in Fig. 6(b)], indicating non-hydrostatic conditions imposed by the argon PTM at these pressures[59] as the cause behind the experimental GeSb- → CrN-type volume compressibility change. On a follow-up reasoning, one might speculate that non-hydrostatic conditions are actually responsible for the displacive GeSb- → CrN-type transitions in both Ag_2ZnSnS_4 and Ag_2CdSnS_4 compounds. Even though we cannot totally exclude this possibility based on our experimental observations alone, the reproducibility of the transitions from our DFT calculations, as well as the good agreement between the theoretical and experimental transition pressures demonstrate that the GeSb- → CrN-type transitions are indeed inherent pressure-induced transitions for both materials.

Finally, in Fig. 6(c), we show the calculated enthalpy difference for the relevant Ag_2CdSnS_4 phases as a function of pressure. The high-pressure GeSb- and CrN-type modifications become energetically stable at 4.7 GPa compared to the starting WZ–KS phase, and the CrN-type phase becomes the stable modification above 12.8 GPa compared to the GeSb-type structure [Fig. 6(d)]. In addition, the calculated structural parameters are consistent with our experimental observations [open symbols in Figs. 6(a) and 6(b)]. Collectively,

our calculations fully endorse the experimental findings for Ag_2CdSnS_4.

IV. DISCUSSION

In the family of the A_2BCX_4 compounds, the only known high-pressure studies concern the ordered and disordered (D)KS Cu_2ZnSnS_4.[35–38] In these investigations, it has been established that pressure transforms (D)KS to a GeSb-type structure close to 15 GPa. Regarding the structural evolution, both the (initially) tetrahedrally coordinated Ag_2ZnSnS_4 and Ag_2CdSnS_4 compounds transform first to a disordered and octahedrally coordinated GeSb-type phase, with further compression leading to a CrN-type modification (an orthorhombically distorted GeSb-type phase). The latter phase was not reported in the case of compressed Cu_2ZnSnS_4. The absence of such a transition in Cu_2ZnSnS_4 might be derived from either the substitution of Cu^+ with the larger Ag^+ cation in Ag_2ZnSnS_4 or Ag_2CdSnS_4, hinting that higher pressures might be needed to detect a similar transition in Cu_2ZnSnS_4, as expected from the empirical pressure-homolog rule.[84]

Even though we cannot provide any information on the exact transition mechanism for either Ag_2ZnSnS_4 or Ag_2CdSnS_4, mainly due to the absence of the relevant structural parameters for the starting KS and WZ–KS phases, we can nevertheless gain some insight by considering the relevant literature. In particular, our observations are consistent within the framework of the relevant binary ZB, WZ,[85,86] and ternary chalcopyrite-type materials,[87–93] where sufficient compression leads to the transformation of the (initially) fourfold structures toward sixfold coordinated phases. An interesting aspect of the relevant transition mechanism in these materials is that they involve an intermediate metastable phase with fourfold coordination,[85,86,94] accompanied by pressure-induced softening in the respective zone-edge TA phonons (see Refs. 86 and 95 and the references therein for more details). Consequently, this intermediate phase facilitating the KS → GeSb-type transition may possibly be the pressure-induced disordering inferred for both Ag_2ZnSnS_4 and Cu_2ZnSnS_4 compounds prior to the GeSb-type transformation. For the WZ–KS Ag_2CdSnS_4 system, on the other hand, no sign of an intermediate phase can be evidenced in our Raman study [Fig. 5(a)]. More investigations will be needed to uncover the exact transition mechanism in these systems.

Upon decompression, a disordered ZB structure is adopted by Ag_2ZnSnS_4 (Fig. 7), similar to Cu_2ZnSnS_4.[35,36] On the contrary, the recovered Ag_2CdSnS_4 could be indexed with a GeSb-type phase, indicating the irreversibility of the sixfold coordinated metallic phase in the latter compound. A possible explanation behind this diversity might involve the presence of the larger Cd^{2+} cation, which is apparently shifting the most favorable packing scheme, leading to different local arrangements, i.e., to sixfold cationic coordination compared to the fourfold one in ZB Ag_2ZnSnS_4/Cu_2ZnSnS_4 containing the smaller Zn^{2+} cations.

An auxiliary aspect of the aforementioned pressure-induced structural transitions in Ag_2ZnSnS_4 and Ag_2CdSnS_4 is the potential effect on their electronic structures. Earlier theoretical investigations[42] have predicted that the respective high-pressure GeSb-type modifications for both Ag_2ZnSnS_4 and Ag_2CdSnS_4 compounds
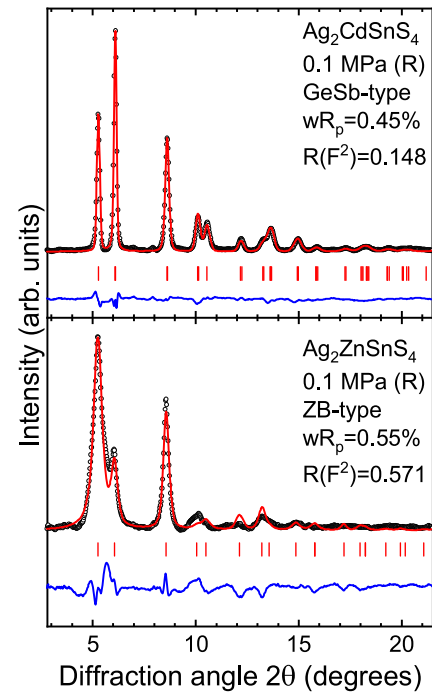

FIG. 7. Rietveld refinements for the recovered XRD patterns for Ag_2ZnSnS_4 (zinc blende/ZB-type structure, bottom) and Ag_2CdSnS_4 (GeSb-type, top). Dots correspond to the experimental data, and the red solid lines represent the best refinements. The difference spectra between the measured and simulated patterns are depicted as blue curves. Vertical ticks mark the respective Bragg peak positions.

exhibit metallic conductivity, i.e., both materials undergo concomitant structural and insulator-to-metal transitions. This trend is again in accordance with the behavior of the binary ZB and WZ compounds.[86,96] Even though we do not have direct experimental evidence of the predicted pressure-induced electronic changes, the loss of Raman signal in the vicinity of the KS/WZ–KS → GeSb-type structural transitions [Figs. 2(a) and 5(a)] can be attributed to the metallic character of the latter phases.[97] For the sake of completeness, we have additionally calculated the electronic density of states (DOS) for the CrN-type structures, which clearly reveal a metallic character for the latter high-pressure Ag_2ZnSnS_4 and Ag_2CdSnS_4 modifications as well (Fig. 8).

A structural aspect that may be essential for technological applications is that compressive stress induces an apparent structural disorder in KS Ag_2ZnSnS_4 at moderate pressures [Figs. 2(c) and S4 in supplementary material]. This observation resembles that of ordered KS Cu_2ZnSnS_4 under moderate compression.[37] Given that (a) disorder in these systems is inherently coupled with their electronic properties[75,98,99] and (b) compressive stresses/strains may arise from the underlying substrates, which may in turn lead to the formation of metastable phases,[31–34] one must consider these aspects carefully for technical thin film applications. Interestingly, certain structural disorder patterns were theoretically tested for Ag_2ZnSnS_4 both at ambient[23] and high pressure,[42] and the stability of the
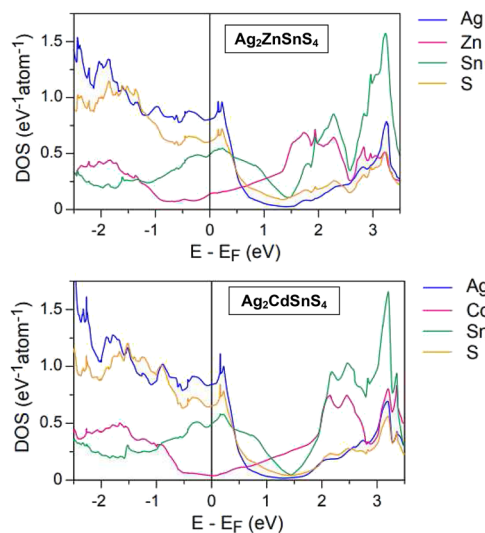
FIG. 8. Site-projected electronic density of states (DOS) calculated for the high-pressure CrN-type modifications of Ag_2ZnSnS_4 (top) and Ag_2CdSnS_4 (bottom).

starting KS structure was shown. Nevertheless, as the nature of the specific disorder process cannot be fully identified, we are not able to discuss this aspect further at this stage.

V. CONCLUSIONS

Our high-pressure Raman and structural investigations on the Ag_2ZnSnS_4 and Ag_2CdSnS_4 compounds revealed that KS Ag_2ZnSnS_4 transforms first into a GeSb-type structure close to 9 GPa, with a subsequent CrN-type modification adopted at 12.5 GPa. In a similar fashion, WZ–KS Ag_2CdSnS_4 undergoes two successive structural transitions toward a GeSb-type and CrN-type phase at ~4 and ~12 GPa, respectively. Our experimental results are fully supported by former[42] and current computations, which additionally predict a metallic character for all of the aforementioned high-pressure modifications.

Except for the follow-up transition to a CrN-type phase, the high-pressure behavior of Ag_2ZnSnS_4 closely resembles that of Cu_2ZnSnS_4.[36,37] Prior to the KS → GeSb-type transition, structural disordering is apparently taking place upon moderate compression. Moreover, Ag_2ZnSnS_4 adopts a disordered zinc blende-type structure upon full decompression. On the contrary, Ag_2CdSnS_4 retains the high-pressure disordered GeSb-type modification upon full pressure release. This deviating behavior may, in turn, inspire a new class of materials synthesized at ambient temperatures upon moderate compression.

SUPPLEMENTARY MATERIAL

See the supplementary material for the characterization of the Ag_2ZnSnS_4 sample investigated here, as well as for additional experimental and calculated data for both Ag_2ZnSnS_4 and Ag_2CdSnS_4 compounds.

AUTHOR DECLARATIONS

Conflict of Interest

The authors have no conflicts to disclose.

Author Contributions

Conceptualization, N.Y.S. and I.E.; methodology, I.E.; experiments, N.Y.S., H.J.R., L.S., S.S.L., and S.S.; synthesis, E.M.H. and M.L.; calculations, E.V., T.K., and B.P. All authors have read and reviewed the manuscript.

Nicole Yvonne Suss: Data curation (equal); Formal analysis (equal); Investigation (lead); Methodology (equal); Validation (equal); Writing – original draft (lead). **Eva M. Heppke**: Resources (lead); Writing – review & editing (equal). **Elena Voloshina**: Investigation (lead); Methodology (equal); Writing – review & editing (equal). **Lukas Schifferle**: Investigation (equal); Writing – review & editing (equal). **Sergey S. Lobanov**: Investigation (equal); Writing – review & editing (equal). **Sergio Speziale**: Investigation (equal); Writing – review & editing (equal). **Hans Josef Reichmann**: Investigation (equal); Writing – review & editing (equal). **Tim Küllmey**: Resources (equal); Writing – review & editing (equal). **Beate Paulus**: Conceptualization (equal); Funding acquisition (equal); Project administration (equal); Writing – review & editing (equal). **Martin Lerch**: Conceptualization (equal); Funding acquisition (equal); Project administration (equal); Resources (equal); Supervision (equal); Writing – review & editing (equal). **Ilias Efthimiopoulos**: Conceptualization (equal); Funding acquisition (equal); Project administration (equal); Writing – review & editing (equal).

DATA AVAILABILITY

The data that support the findings of this study are available within the article and its supplementary material.

REFERENCES

[1] T. Gershon, Y. S. Lee, P. Antunez, R. Mankad, S. Singh, D. Bishop, O. Gunawan, M. Hopstaken, and R. Haight, Adv. Energy Mater. **6**, 1502468 (2016).
[2] S. Giraldo, Z. Jehl, M. Placidi, V. Izquierdo-Roca, A. Perez-Rodriguez, and E. Saucedo, Adv. Mater. **31**, 1806692 (2019).

31 October 2023 05:52:40

[3] H. Katagiri, K. Jimbo, W. S. Maw, K. Oishi, M. Yamazaki, H. Araki, and A. Takeuchi, Thin Solid Films **517**, 2455 (2009).

[4] S. Siebentritt and S. Schorr, Prog. Photovoltaics **20**, 512 (2012).

[5] A. Wang, M. He, M. A. Green, K. Sun, and X. Hao, Adv. Energy Mater. **13**, 2203046 (2023).

[6] K. Yu and E. A. Carter, Chem. Mater. **27**, 2920 (2015).

[7] C. Yan, J. Huang, K. Sun, S. Johnston, Y. Zhang, H. Sun, A. Pu, M. He, F. Liu, K. Eder, L. Yang, J. M. Cairney, N. J. Ekins-Daukes, Z. Hameiri, J. A. Stride, S. Chen, M. A. Green, and X. Hao, Nat. Energy **3**, 764 (2018).

[8] J. T. Armstrong, Microbeam Anal. **4**, 177 (1995).

[9] C. Rincon, E. Quintero, M. Quintero, E. Moreno, C. Power, M. Morocoima, and G. E. Delgado, Phys. Status Solidi B **256**, 1900076 (2019).

[10] H. Oueslati, M. Ben Rabeh, J. Martin, and M. Kanzari, Thin Solid Films **669**, 633 (2019).

[11] T. H. Nguyen, T. Kawaguchi, J. Chantana, T. Minemoto, T. Harada, S. Nakanishi, and S. Ikeda, ACS Appl. Mater. Interfaces **10**, 5455 (2018).

[12] K. Rudisch, A. Davydova, C. Platzer-Bjorkman, and J. Scragg, J. Appl. Phys. **123**, 161558 (2018).

[13] C. J. Bosson, M. T. Birch, D. P. Halliday, C. C. Tang, A. K. Kleppe, and P. D. Hatton, Chem. Mater. **29**, 9829 (2017).

[14] M. Dimitrievska, F. Boero, A. P. Litvinchuk, S. Delsante, G. Borzone, A. Perez-Rodriguez, and V. Izquierdo-Roca, Inorg. Chem. **56**, 3467 (2017).

[15] N. Y. Suss, E. M. Heppke, F. D. Avci, O. Appelt, and I. Efthimiopoulos, Z. Naturforsch. B **77**, 425 (2022).

[16] T. Shibuya, Y. Goto, Y. Kamihara, M. Matoba, K. Yasuoka, L. A. Burton, and A. Walsh, Appl. Phys. Lett. **104**, 21912 (2014).

[17] C. Wang, S. Chen, J. H. Yang, L. Lang, H. J. Xiang, X. G. Gong, A. Walsh, and S. H. Wei, Chem. Mater. **26**, 3411 (2014).

[18] A. Bhattacharya, D. G. Tkachuk, A. Mar, and V. K. Michaelis, Chem. Mater. **33**, 4709 (2021).

[19] E. M. Heppke, S. Klenner, O. Janka, R. Pöttgen, T. Bredow, and M. Lerch, Inorg. Chem. **60**, 2730 (2021).

[20] D. Payno, S. Kazim, and S. Ahmad, J. Mater. Chem. C **9**, 17392 (2021).

[21] E. M. Heppke, S. Mahadevan, T. Bredow, and M. Lerch, Z. Naturforsch. B **76**, 607 (2021).

[22] E. M. Heppke and M. Lerch, Z. Naturforsch. B **75**, 721 (2020).

[23] P. Mangelis, A. Aziz, I. da Silva, R. Grau-Crespo, P. Vaqueiro, and A. V. Powell, Phys. Chem. Chem. Phys. **21**, 19311 (2019).

[24] J. Li, D. Wang, X. Li, Y. Zeng, and Y. Zhang, Adv. Sci. **5**, 1700744 (2018).

[25] J. J. S. Scragg, J. K. Larsen, M. Kumar, C. Persson, J. Sendler, S. Siebentritt, and C. Platzer Björkman, "Cu-Zn disorder and band gap fluctuations in Cu$_2$ZnSn(S,Se)$_4$: Theoretical and experimental investigations: Cu-Zn disorder and band gap fluctuations in Cu$_2$ZnSn(S,Se)$_4$," Phys. Status Solidi B **253**, 247 (2016).

[26] E. M. Heppke, T. Kullmey, I. Efthimiopoulos, F. D. Avci, O. Appelt, B. Paulus, and M. Lerch, Mater. Res. Express **6**, 125525 (2019).

[27] W. Li, X. Liu, H. Cui, S. Huang, and X. Hao, J. Alloys Compd. **625**, 277 (2015).

[28] A. Guchhait, Z. Su, Y. F. Tay, S. Shukla, W. Li, S. W. Leow, J. M. R. Tan, S. Lie, O. Gunawan, and L. H. Wong, ACS Energy Lett. **1**, 1256 (2016).

[29] Z. K. Yuan, S. Chen, H. Xiang, X. G. Gong, A. Walsh, J. S. Park, I. Repins, and S. H. Wei, Adv. Funct. Mater. **25**, 6733 (2015).

[30] W. Gong, T. Tabata, K. Takei, M. Morihama, T. Maeda, and T. Wada, Phys. Status Solidi C **12**, 700 (2015).

[31] M. Chhowalla and H. E. Unalan, Nat. Mater. **4**, 317 (2005).

[32] D. R. McKenzie, D. Muller, and B. A. Pailthorpe, Phys. Rev. Lett. **67**, 773 (1991).

[33] P. A. Gabrys, S. E. Seo, M. X. Wang, E. Oh, R. J. Macfarlane, and C. A. Mirkin, Nano Lett. **18**, 579 (2018).

[34] H. Köstenbauer, G. A. Fontalvo, M. Kapp, J. Keckes, and C. Mitterer, Surf. Coat. Technol. **201**, 4777 (2007).

[35] I. Efthimiopoulos, T. Kullmey, S. Speziale, A. S. Pakhomova, M. Quennet, B. Paulus, A. Ritscher, and M. Lerch, Appl. Phys. A **127**, 616 (2021).

[36] I. Efthimiopoulos, T. Kullmey, S. Speziale, A. S. Pakhomova, M. Quennet, B. Paulus, A. Ritscher, M. Lerch, and M. Koch-Muller, J. Appl. Phys. **124**, 085905 (2018).

[37] I. Efthimiopoulos, A. Ritscher, M. Lerch, S. Speziale, A. S. Pakhomova, H. P. Liermann, and M. Koch-Muller, Appl. Phys. Lett. **110**, 041905 (2017).

[38] S. P. Kandare, B. Joseph, M. N. Rao, S. S. Dahiwale, S. D. Dhole, and R. Rao, J. Alloys Compd. **867**, 159041 (2021).

[39] B. Ananthoju, J. Mohapatra, M. K. Jangid, D. Bahadur, N. V. Medhekar, and M. Aslam, Sci. Rep. **6**, 35369 (2016).

[40] S. Chen, X. G. Gong, A. Walsh, and S.-H. Wei, Appl. Phys. Lett. **94**, 041903 (2009).

[41] M. D. K. Jones, J. A. Dawson, S. Campbell, V. Barrioz, L. D. Whalley, and Y. Qu, Front. Chem. **10**, 920676 (2022).

[42] T. Küllmey, J. Hein, E. M. Heppke, I. Efthimiopoulos, and B. Paulus, ACS Omega **6**, 27387 (2021).

[43] T. Jing, Y. Dai, X. Ma, W. Wei, and B. Huang, J. Phys. Chem. C **119**, 27900 (2015).

[44] T. Sasamura, T. Osaki, T. Kameyama, T. Shibayama, A. Kudo, S. Kuwabata, and T. Torimoto, Chem. Lett. **41**, 1009 (2012).

[45] K. Li, B. Chai, T. Peng, J. Mao, and L. Zan, RSC Adv. **3**, 253 (2013).

[46] K. W. Cheng and S. W. Hong, ACS Appl. Mater. Interfaces **10**, 22130 (2018).

[47] K. Pietak, C. Jastrzebski, K. Zberecki, D. J. Jastrzebski, W. Paszkowicz, and S. Podsiadlo, J. Solid State Chem. **290**, 121467 (2020).

[48] S. Schorr, Thin Solid Films **515**, 5985 (2007).

[49] G. E. Davydyuk, G. L. Myronchuk, I. Kityk, S. P. Danylchuk, V. Bozhko, and O. Parasyuk, Opt. Mater. **33**, 1302 (2011).

[50] E. M. Heppke, S. Berendts, and M. Lerch, Z. Naturforsch. B **75**, 393 (2020).

[51] K. Syassen, High Pressure Res. **28**, 75 (2008).

[52] M. Y. Valakh, V. M. Dzhagan, I. S. Babichuk, X. Fontane, A. Perez-Rodriguez, and S. Schorr, JETP Lett. **98**, 255 (2013).

[53] M. Wojdyr, J. Appl. Crystallogr. **43**, 1126 (2010).

[54] H.-P. Liermann, Z. Konopkova, W. Morgenroth, K. Glazyrin, J. Bednarcik, E. E. McBride, S. Petitgirard, J. T. Delitz, M. Wendt, Y. Bican, A. Ehnes, I. Schwark, A. Rothkirch, M. Tischer, J. Heuer, H. Schulte-Schrepping, T. Kracht, and H. Franz, J. Synchrotron Radiat. **22**, 908 (2015).

[55] A. P. Hammersley, S. O. Svensson, M. Hanfland, A. N. Fitch, and D. Hausermann, High Pressure Res. **14**, 235 (1996).

[56] B. H. Toby, J. Appl. Crystallogr. **34**, 210 (2001).

[57] F. Birch, J. Geophys. Res. **83**, 1257, https://doi.org/10.1029/jb083ib03p01257 (1978).

[58] F. Birch, Phys. Rev. **71**, 809 (1947).

[59] S. Klotz, J.-C. Chervin, P. Munsch, and G. Le Marchand, J. Phys. D: Appl. Phys. **42**, 075413 (2009).

[60] M. Ross, H. K. Mao, P. M. Bell, and J. A. Xu, J. Chem. Phys. **85**, 1028 (1986).

[61] D. Errandonea, R. Boehler, S. Japel, M. Mezouar, and L. R. Benedetti, Phys. Rev. B **73**, 092106 (2006).

[62] G. Kresse and J. Furthmüller, Phys. Rev. B **54**, 11169 (1996).

[63] G. Kresse and D. Joubert, Phys. Rev. B **59**, 1758 (1999).

[64] J. P. Perdew, K. Burke, and M. Ernzerhof, Phys. Rev. Lett. **77**, 3865 (1996).

[65] P. E. Blöchl, Phys. Rev. B **50**, 17953 (1994).

[66] P. E. Blöchl, O. Jepsen, and O. K. Andersen, Phys. Rev. B **49**, 16223 (1994).

[67] A. Khare, B. Himmetoglu, M. Johnson, D. J. Norris, M. Cococcioni, and E. S. Aydil, J. Appl. Phys. **111**, 083707 (2012).

[68] C. Ma, H. Guo, K. Zhang, N. Yuan, and J. Ding, Mater. Lett. **186**, 390 (2017).

[69] J. Kumar and S. Ingole, J. Alloys Compd. **865**, 158113 (2021).

[70] M. Guc, S. Levcenko, I. V. Bodnar, V. Izquierdo-Roca, X. Fontane, L. V. Volkova, E. Arushanov, and A. Perez-Rodriguez, Sci. Rep. **6**, 19414 (2016).

[71] S. P. Ramkumar, G. Petretto, W. Chen, H. P. C. Miranda, X. Gonze, and G.-M. Rignanese, Phys. Rev. Mater. **6**, 035403 (2022).

[72] J. M. Skelton, A. J. Jackson, M. Dimitrievska, S. K. Wallace, and A. Walsh, APL Mater. **3**, 041102 (2015).

[73] M. Y. Valakh, O. F. Kolomys, S. S. Ponomaryov, V. O. Yukhymchuk, I. S. Babichuk, V. Izquierdo-Roca, E. Saucedo, A. Perez-Rodriguez, J. R. Morante, S. Schorr, and I. V. Bodnar, Phys. Status Solidi RRL **7**, 258 (2013).

[74] R. Caballero, E. Garcia-Llamas, J. M. Merino, M. Leon, I. Babichuk, V. Dzhagan, V. Strelchuk, and M. Valakh, Acta Mater. **65**, 412 (2014).

[75] S. Schorr, G. Gurieva, M. Guc, M. Dimitrievska, A. Perez-Rodriguez, V. Izquierdo-Roca, C. S. Schnohr, J. Kim, W. Jo, and J. M. Merino, J. Phys. Energy **2**, 012002 (2020).

[76] L. M. Corliss, N. Elliott, and J. M. Hastings, Phys. Rev. **117**, 929 (1960).

[77] E. Kroumova, M. I. Aroyo, J. Perez-Mato, A. Kirov, C. Capillas, S. Ivantchev, and H. Wondratschek, Phase Transit. **76**, 155 (2003).

[78] S. Baroni, S. de Gironcoli, A. Dal Corso, and P. Giannozzi, Rev. Mod. Phys. **73**, 515 (2001).

[79] O. Brafman and S. S. Mitra, Phys. Rev. **171**, 931 (1968).

[80] Y. C. Cheng, C. Q. Jin, F. Gao, X. L. Wu, W. Zhong, S. H. Li, and P. K. Chu, J. Appl. Phys. **106**, 123505 (2009).

[81] J. Schneider and R. D. Kirby, Phys. Rev. B **6**, 1290 (1972).

[82] Y. Ebisuzaki and M. Nicol, J. Phys. Chem. Solids **33**, 763 (1972).

[83] J. Serrano, A. Cantarero, M. Cardona, N. Garro, R. Lauck, R. E. Tallman, T. M. Ritter, and B. A. Weinstein, Phys. Rev. B **69**, 014301 (2004).

[84] A. Neuhaus, Chimia **18**, 93 (1964).

[85] M. S. Miao and W. R. L. Lambrecht, Phys. Rev. Lett. **94**, 225501 (2005).

[86] A. Mujica, A. Rubio, A. Munoz, and R. J. Needs, Rev. Mod. Phys. **75**, 863 (2003).

[87] D. Errandonea, R. S. Kumar, O. Gomis, F. J. Manjon, V. V Ursaki, and I. M. Tiginyanu, J. Appl. Phys. **114**, 233507 (2013).

[88] D. Errandonea, R. S. Kumar, F. J. Manjon, V. V Ursaki, and I. M. Tiginyanu, J. Appl. Phys. **104**, 063524 (2008).

[89] T. Tinoco, A. Polian, D. Gomez, and J. P. Itie, Phys. Status Solidi B **198**, 433 (1996).

[90] T. Tinoco, A. Polian, J. P. Itie, E. Moya, and J. Gonzalez, J. Phys. Chem. Solids **56**, 481 (1995).

[91] V. V. Ursaki, I. I. Burlakov, I. M. Tiginyanu, Y. S. Raptis, E. Anastassakis, and A. Anedda, Phys. Rev. B **59**, 257 (1999).

[92] V. S. Bhadram, L. Krishna, E. S. Toberer, R. Hrubiak, E. Greenberg, V. B. Prakapenka, and T. A. Strobel, Appl. Phys. Lett. **110**, 182106 (2017).

[93] A. Werner, H. D. Hochheimer, and A. Jayaraman, Phys. Rev. B **23**, 3836 (1981).

[94] M. Catti, Phys. Rev. B **65**, 224115 (2002).

[95] B. A. Weinstein, Phys. Rev. B **104**, 054105 (2021).

[96] G. A. Samara and H. G. Drickamer, J. Phys. Chem. Solids **23**, 457 (1962).

[97] A. F. Goncharov and V. V. Struzhkin, J. Raman Spectrosc. **34**, 532 (2003).

[98] S. Chen, X. G. Gong, A. Walsh, and S. H. Wei, Appl. Phys. Lett. **96**, 021902 (2010).

[99] S. Chen, A. Walsh, X.-G. Gong, and S.-H. Wei, Adv. Mater. **25**, 1522 (2013).